ADVANCED FUNCTIONAL MATERIALS
www.afm-journal.de

Check for updates

Ultrafast Responsive Non-Volatile Flash Photomemory via Spatially Addressable Perovskite/Block Copolymer Composite Film

*Yu-Hsiang Chang, Chia-Wei Ku, Yi-Hua Zhang, Hsiang-Chen Wang, and Jung-Yao Chen**

The exotic photophysical properties of organic–inorganic hybrid perovskite with long exciton lifetimes and small binding energy have appeared as promising front-runners for next-generation non-volatile flash photomemory. However, the long photo-programming time of photomemory limits its application on light-fidelity (Li-Fi), which requires high storage capacity and short programming times. Herein, the spatially addressable perovskite in polystyrene-*block*-poly(ethylene oxide) (PS-*b*-PEO)/perovskite composite film as an photoactive floating gate is demonstrated to elucidate the effect of morphology on the photo-responsive characteristics of photomemory. The chelation between lead ion and PEO segment promotes the anti-solvent functionalities of the perovskite/PS-*b*-PEO composite film, thus allowing the solution-processable poly(3-hexylthiophene-2,5-diyl) (P3HT) to act as the active channel. Through manipulating the interfacial area between perovskite and P3HT, fast photo-induced charge transfer rate of 0.056 ns^{-1}, high charge transfer efficiency of 89%, ON/OFF current ratio of 10^4, and extremely low programming time of 5 ms can be achieved. This solution-processable and fast photo-programmable non-volatile flash photomemory can trigger the practical application on Li-Fi.

1. Introduction

Light fidelity (Li-Fi) is a next-generation communication system with the features of high security, high speed, and low interference. Corresponding devices such as light-emitting diodes (LEDs), image sensors, photocoupler, photodiodes, and non-volatile flash photomemory should be explored.[1,2] Among the plethora of derivatives in optical communications, non-volatile flash photomemory is of particular interest since it is the essential building block of computation technology for current big database storage device. Based on the similar principle of transistor-type memory which uses spatially confined metallic or semiconducting floating-gate elements as charge-trapping site to electrically isolate trapped charges from the surrounding insulator, charge trapping/storing can be created using photon instead of electrical field.[3–8] The photon can program the device by photo-exciting the photoactive material and then dissociating the photo-generated exciton at the interfaces between photoactive material and active channel. Large ON/OFF current ratio, long-term storage, and short photo-programming time are essential to ensure the non-volatile flash photomemory as the substitute of electric-programming one. Yet, to date, there have been limited systematic studies of photomemory that address the photo-programming time for effective programming process.[9–11]

The exceptional semiconducting properties of organic–inorganic hybrid perovskite materials, such as long exciton lifetime and small binding energy, have appeared as promising front-runners for next-generation non-volatile flash photomemory.[12–19] Our previous research work has demonstrated the perovskite/polystyrene (PS) composite film based photomemory with wavelength/illumination power/illumination time distinguishable functionalities under the absence of vertical electrical field.[20] Through blending with different host insulating polymers, the photoresponse behavior and the resultant ON/OFF current ratio increases as the amount of perovskite nanoparticles on the surface of perovskite/insulating polymer composite film increases due to the enhanced interfacial photo-induced charge transfer across the perovskite/active channel interface.[21] The high capacity of perovskite in the optoelectronics generally provides high photo-induced current during photo-to-electric effect and large particle size with long exciton lifetime. However, excess perovskite in the insulating polymer matrix may lead to a continuous passage in the charge-trapping layer and thus deteriorate the retention capability. Therefore, increasing the amount of perovskite in photoactive composite film while preserving the isolated barrier around perovskite seems to be the next challenge on the application of non-volatile flash memory.

Block copolymer (BCP) with unique phase separation behavior have facilitated the supramolecular self-assembly for

Y.-H. Chang, C.-W. Ku, Y.-H. Zhang, Prof. J.-Y. Chen
Department of Chemical Engineering and Advanced Institute of Manufacturing with High-tech Innovations
National Chung Cheng University
Chiayi 62102, Taiwan
E-mail: chmjyc@ccu.edu.tw
Prof. H.-C. Wang
Department of Mechanical Engineering and Advanced Institute of Manufacturing with High-tech Innovations
National Chung Cheng University
Chiayi 62102, Taiwan
The ORCID identification number(s) for the author(s) of this article can be found under https://doi.org/10.1002/adfm.202000764.

DOI: 10.1002/adfm.202000764

 © 2020 WILEY-VCH Verlag GmbH & Co. KGaA, Weinheim

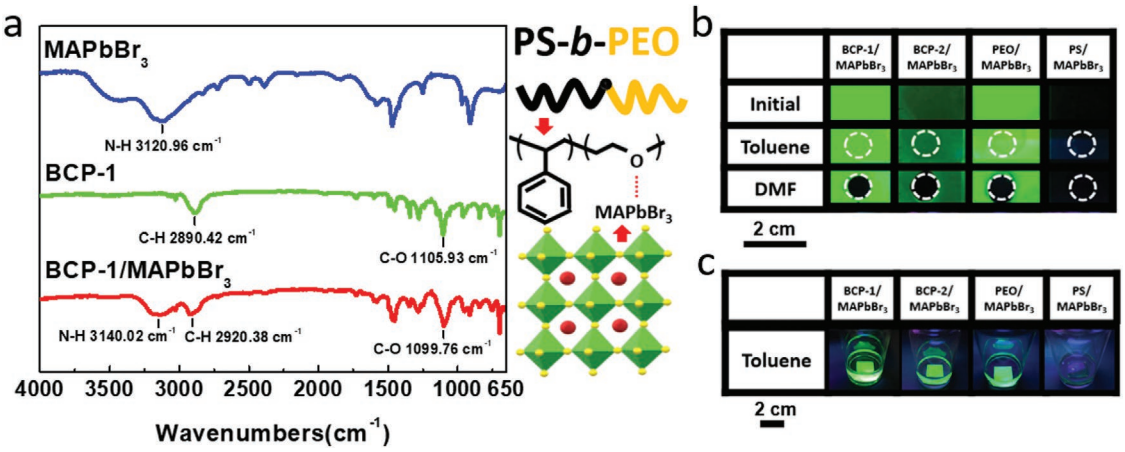

Figure 1. a) FTIR spectra of the pristine BCP-1 and $MAPbBr_3$ and BCP-1/$MAPbBr_3$ composite film. b) Anti-solvent characteristics of BCP-1/$MAPbBr_3$, BCP-2/$MAPbBr_3$, PEO/$MAPbBr_3$, and PS/$MAPbBr_3$ composite films at the initial state and under toluene and DMF drop test where white dot circle demonstrated the solvent drop. The scale bar is 2 cm. c) Anti-solvent stability test of BCP-1/$MAPbBr_3$, BCP-2/$MAPbBr_3$, PEO/$MAPbBr_3$, and PS/$MAPbBr_3$ composite films in toluene. The scale bar is 2 cm.

the in situ preparation of metallic or semiconducting nanostructure in amphiphilic block copolymers.[22–26] The one-step solution process for generating arrays of nanostructure makes this approach amenable to the field of non-volatile memory due to the high charge-storage capacity and permanent storage capability.[25–27] However, even though the spatially defined perovskite nanostructure through selectively noncovalent bond to one segment of block copolymers has attracted widespread interest, especially in the field of photo-physic and LED application,[28–33] the morphological effects of block copolymer/perovskite composite film on the photo-responsive characteristics of non-volatile flash photomemory remain undeveloped.

We demonstrate herein, for the first time, a non-volatile flash photomemory comprising an in situ synthesis strategy of perovskite nanostructure in polystyrene-*block*-poly(ethylene oxide) (PS-*b*-PEO) as photo-active floating gate. The anti-solvent properties of PS-*b*-PEO/perovskite composite film make the solution-processable poly(3-hexylthiophene-2,5-diyl) (P3HT) as an active channel. Through manipulating the interfacial area between perovskite and P3HT by the volume fraction of PS and PEO segments, the photo-responsive characteristics of non-volatile flash photomemory, such as photo-response current, charge transfer rate, and photo-programming time were systemically investigated.

Given its coordinated effect on the perovskite surface, PEO has aroused widespread interest on defect passivation and device stability of perovskite-related optoelectronics.[34–36] Thus, the photoactive floating-gate composed of PS-*b*-PEO as the template for spatially addressable perovskite was studied here to elucidate its morphological effect on the photo-responsive features of photomemory. Two asymmetric linear block copolymers coded as BCP-1(PS_{24k}-*b*-PEO_{21k}) and BCP-2 (PS_{114k}-*b*-PEO_{31k}) and two corresponding homopolymer PEO and PS have been selected as matrix to disperse perovskite. The corresponding insulating/perovskite composite films were named as BCP-1/$MAPbBr_3$, BCP-2/$MAPbBr_3$, PEO/$MAPbBr_3$, and PS/$MAPbBr_3$ in the following.

2. Results and Discussion

2.1. Morphological Analysis

To investigate the interaction between $MAPbBr_3$ and PEO segmental matrix in the BCP, Fourier transform infrared spectroscopy (FTIR) spectra in the range of 650–4000 cm^{-1} for $MAPbBr_3$, BCP-1, and BCP-1/$MAPbBr_3$ were performed (**Figure 1**a). The peak for the stretching vibrations of the C—O bond shifted from 1105.93 cm^{-1} in the pristine BCP film to 1099.76 cm^{-1} in the BCP-1/$MAPbBr_3$ composite film. This shift reveals that the precursor Pb^{2+} ions preferentially coordinate with oxygen in the PEO unit of BCP via the Lewis acid–base interaction.[34–36] Benefiting from the strong interaction between PEO and lead ion, the BCP/$MAPbBr_3$ composite film demonstrated superior anti-solvent functionality. Toluene, the good solvent for BCP, PEO, and PS, was dropped on the BCP-1/$MAPbBr_3$, BCP-2/$MAPbBr_3$, PEO/$MAPbBr_3$, and PS/$MAPbBr_3$ as shown in Figure 1b. It should be noted that due to the high solubility of BCP in toluene, the wetting part of pure BCP-1 film was destroyed during toluene dropping test (Figure S1, Supporting Information). Interestingly, all the composite films under UV-light illumination remained intact and emitted green light homogeneously, demonstrating the strong coordinated interaction between perovskite and the polymers and proving that perovskite is the quasi-crosslinker in the composite film. The above assumption can be further proven through dimethylformamide (DMF) dropping test. Given the high solubility of perovskite and polymer in DMF, all composite films were destroyed and show dimmed light in the DMF dropping area. More importantly, after immersing in toluene for 1 day (Figure 1c), all composite films remained intact and stable. The superior anti-solvent feature of all composite films enabled the solution-processable poly(3-hexylthiophene-2,5-diyl) (P3HT) as the active channel and thus extended the photoresponsivity of perovskite-based photomemory to red-light region due to the high absorption of P3HT in the region from 530 to 660 nm (Figure 3b), which will be discussed in

© 2020 WILEY-VCH Verlag GmbH & Co. KGaA, Weinheim

electrical properties of studied photomemory. Besides, it should be noted that the light-emitting intensity of the composite films seems to rely on the content of PEO segment in the polymer matrix, which may result from the effect of defect passivation from PEO and thus inhibition of the non-radiative recombination of perovskite.[35]

Figure S2a,b, Supporting Information, presents the scanning electron microscopy (SEM) images of BCP-1/$MAPbBr_3$ and BCP-2/$MAPbBr_3$, respectively, wherein no large-particle perovskites were found on the surface of composite films, indicating that the geometric confinement of perovskite in BCP can be realized through the interaction between PEO and perovskite even under high perovskite content. Conversely, the severe aggregation of perovskite on the surface of PS/$MAPbBr_3$ and PEO/$MAPbBr_3$ composite film can be clearly observed in Figures S2c and S2d, Supporting Information, respectively. Large particles or even network structure may deteriorate the isolation effect from polymer and provide a passage for the trapped charge-carrier in the relevant photomemory, which will be discussed later. The morphology and crystallinity of $MAPbBr_3$ in the hybrid film were further characterized by transmission electron microscopy (TEM). The symmetric BCP-1 with PEO volume fraction (f_{PEO}) of 45% theoretically tends to form lamellar structures; however, due to the high concentration of perovskite in BCP-1/$MAPbBr_3$, PS self-organized into vertical aligned cylinders in the PEO/$MAPbBr_3$ matrix as shown in **Figure 2**a, where the dark region corresponds to the PEO domains incorporating the $MAPbBr_3$ crystals. On the other hand, the highly asymmetric PS-*b*-PEO with f_{PEO} of 20% in BCP-2/$MAPbBr_3$ showed theoretical PEO/$MAPbBr_3$ sphere nanodomains even impregnated with a high concentration of perovskite (Figure 2b). The difference in the distribution of perovskite nanodomain by the two volume fraction of BCP (PEO/$MAPbBr_3$ matrix with vertical PS cylinders in BCP-1/$MAPbBr_3$ and PS matrix with PEO/$MAPbBr_3$ spheres in BCP-2/$MAPbBr_3$) greatly affected the photo-responsive properties of the corresponding photomemory as described below.

Grazing incidence wide-angle x-ray scattering (GIWAXS) was implemented to investigate the crystal structures of perovskite embedded in the composite film. As shown in Figure 2c,d and Figure S3, Supporting Information, all 2D GIWAXS patterns of the composite films exhibited diffraction peaks at q_{xy} = 1.067 and 1.514 $Å^{-1}$ corresponding to the (1 0 0) and (1 1 0) planes of the cubic $MAPbBr_3$ crystalline structure, respectively, and indicating the successful formation of perovskite inside the composite films.

Grazing-incident small-angle X-ray scattering (GISAXS) was conducted to acquire information about the morphologies of the BCP/$MAPbBr_3$ composite thin films. Figure S4a,b, Supporting Information, shows the 2D GISAXS patterns of BCP-1/$MAPbBr_3$ and BCP-2/$MAPbBr_3$ thin films annealed in benzene vapor for 17 h. The GISAXS profile for the BCP-1/$MAPbBr_3$ and BCP-2/$MAPbBr_3$ 2D thin film showed reflections at the in-plane scattering vectors at q_y = 0.011 and q_y = 0.008 $Å^{-1}$, respectively (Figure 2e,f), and the domain spacing can be estimated from the scattering vector at first-order peak. The domain spacing of cylinder-to-cylinder was found to be 57 nm in BCP-1/$MAPbBr_3$ and the PEO/$MAPbBr_3$ spheres in BCP-2/ $MAPbBr_3$ increased to 78 nm, which are consistent with the TEM results.

2.2. Device Fabrication and Optical Analysis

To explore the morphological effect of perovskite on the photo-responsive characteristics of photomemory, the perovskite-based photomemories were studied here and the device configuration with BCP/$MAPbBr_3$ composite film as photo-induced charge-trapping layer and P3HT as active channel is shown in **Figure 3**a. Figure 3b shows the UV–visible absorption spectra of the BCP/$MAPbBr_3$ composite films and the P3HT film. As can be seen, the composite film and the P3HT film featured wide absorption bands with a band edge of about 530 nm for composite films and 660 nm for P3HT film. The estimated optical band gaps were approximately 2.2 and 1.9 eV for composite films and P3HT film, respectively. These results support that the P3HT with the highest occupied molecular orbital (HOMO) level of 5.0 eV and lowest unoccupied molecular orbital (LUMO) level of 3.1 eV was selected as the active channel material since its energy levels are appropriate to the values (HOMO: 5.6 eV and LUMO: 3.4 eV) of $MAPbBr_3$ to ensure efficient charge transfer between them.[20] Further observation showed that the absorption spectrum of BCP/$MAPbBr_3$ ranged from 300 to 550 nm, while P3HT absorption occurred in the spectral coverage range of 350–660 nm. The complementary absorption spectra enabled the light storage in visible light for the corresponding photomemories.

To confirm the charge-transfer capability between the BCP/$MAPbBr_3$ composite films and P3HT, steady-state photoluminescence (PL) measurement was explored. The quenching of PL intensity supports the photo-induced charge-carrier transfer between two species in conjunction. Therefore, if the photo-induced charge-carrier is transferred from the perovskite to the P3HT active layer, then electron and hole in the perovskite cannot recombine, thus weakening light emission. Figure 3c,d shows the PL spectra of the BCP-1/$MAPbBr_3$ and BCP-2/$MAPbBr_3$ composite films deposited on quartz and P3HT, respectively. All composite films on P3HT were quenched by over 90% with respect to the PL intensity of one on quartz which prove the photo-induced hole transfer from the perovskite to the active layer.

The cryogenic PL was implemented to evaluate the exciton binding energy of perovskite before and after photo-induced charge transfer. **Figure 4** illustrates the pseudocolor maps and fitting curves of the temperature-dependent PL spectra within the temperature range of 10–300 K for BCP/$MAPbBr_3$ and BCP/$MAPbBr_3$/P3HT. As shown in Figure 4c, the intensity of the integrated PL (from Figure 4a,b) is a temperature-dependent parameter and Equation (1) can be used to describe this phenomenon.

$$I(T) = \frac{I_0}{1 + Ae^{-E_b/k_BT}} \tag{1}$$

where I_0 is the intensity at 0 K, T is the temperature, E_b is the exciton binding energy of perovskite, A is the scaling constant, and k_B is Boltzmann constant. The integrated PL intensity slightly decreased with increasing temperature. In this study, the exciton binding energy of perovskite was evaluated by fitting the high temperature (90–300 K) spectroscopic results. Based on the fitting curves, BCP-1/$MAPbBr_3$ has an exciton binding energy (E_b) of 101.85 meV, whereas BCP-1/$MAPbBr_3$/P3HT shows an E_b of 87.10 meV. Figure 4f shows the integrated PL intensity

© 2020 WILEY-VCH Verlag GmbH & Co. KGaA, Weinheim

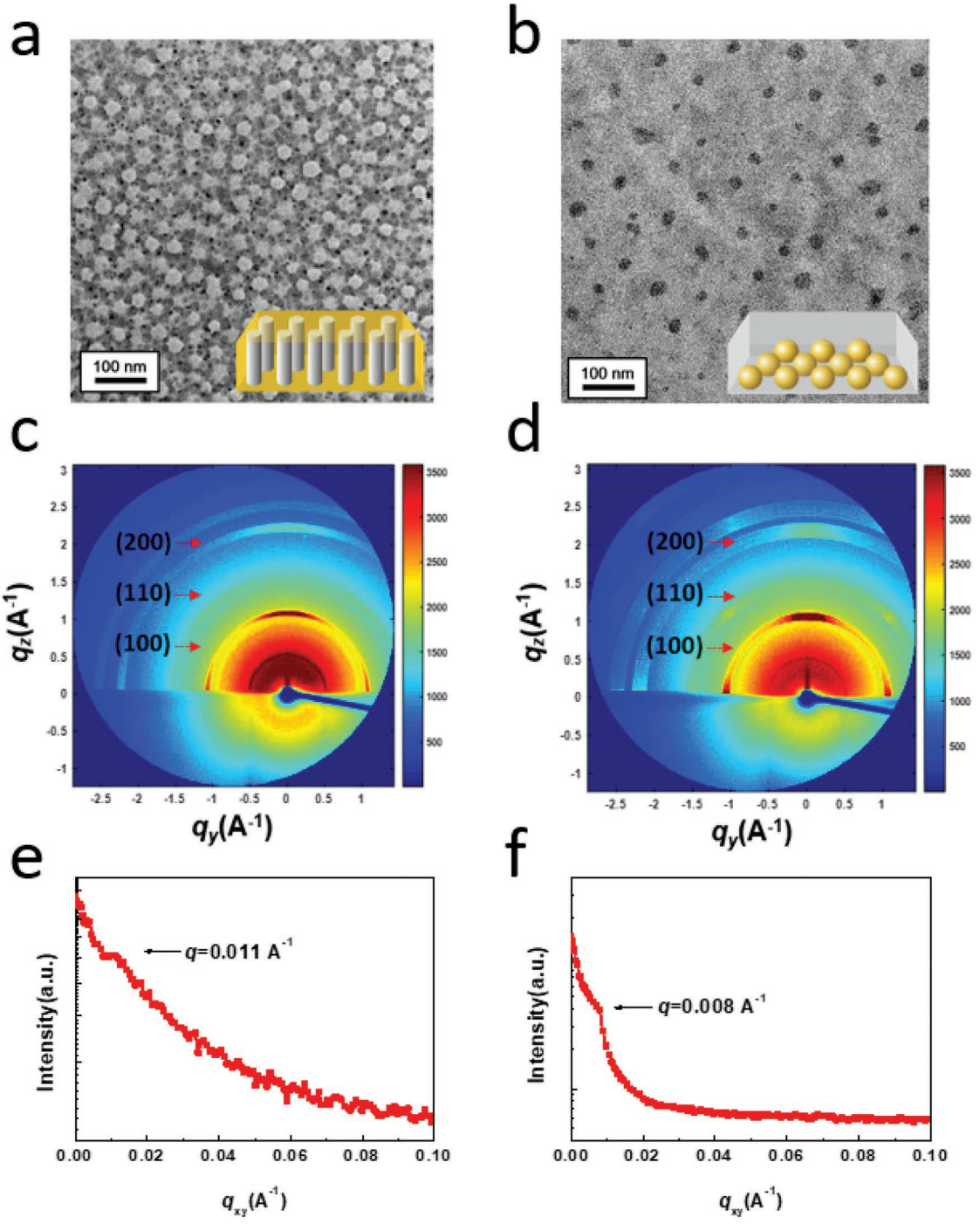

Figure 2. TEM images of a) BCP-1/$MAPbBr_3$ and b) BCP-2/$MAPbBr_3$ composite films after annealing for 17 h in benzene vapor. GIWAXS 2D pattern of c) BCP-1/$MAPbBr_3$ and d) BCP-2/$MAPbBr_3$ composite films. The GISAXS profiles of e) BCP-1/$MAPbBr_3$ and f) BCP-2/$MAPbBr_3$ composite films.

(from Figure 4d,e) for BCP-2/$MAPbBr_3$ with E_b of 104.79 meV, while the BCP-2/$MAPbBr_3$/P3HT shows an E_b of 84.75 meV. The decreased exciton binding energy of BCP/$MAPbBr_3$/P3HT with respect to the BCP/$MAPbBr_3$ further implies the photo-induced charge storage inside the $MAPbBr_3$, which increased the permittivity of $MAPbBr_3$ and consequently decreased the E_b of $MAPbBr_3$.

2.3. Performance of Perovskite-Based Photomemory

To investigate the charge-trapping capability of these studied hybrid layers, the *I–V* characteristics were recorded by sweeping the gate voltage (V_{GS}) between 20 and –60 V under a fixed drain voltage (V_{DS}) of –60 V as shown in **Figure 5**a,b. Both BCP-1/$MAPbBr_3$ and BCP-2/$MAPbBr_3$ based photomemories

© 2020 WILEY-VCH Verlag GmbH & Co. KGaA, Weinheim

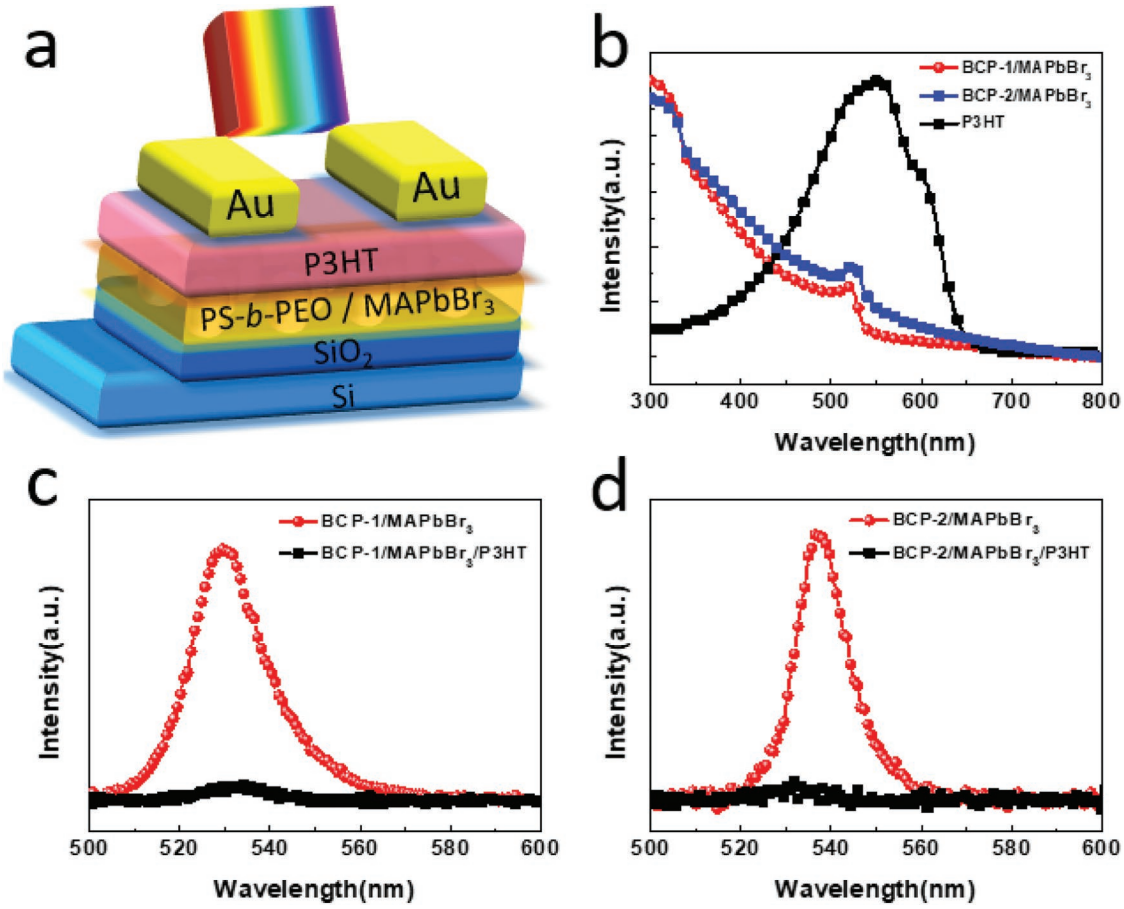

Figure 3. a) Schematic image of the studied photomemory devices. b) Optical absorption spectra of the P3HT film and the BCP/$MAPbBr_3$ composite films. PL of the composite films on quartz and on P3HT with excitation at 450 nm for c) BCP-1/$MAPbBr_3$ and d) BCP-2/$MAPbBr_3$, respectively.

show typical field-effect modulation current with ON/OFF current ratios of 4.07×10^4 and 8.15×10^3, respectively, implying that the typical P3HT thin film based field-effect transistor can be successfully prepared with the anti-solvent characteristic of BCP/$MAPbBr_3$ composite film as the underlying dielectric layer. After green-light illumination (520 nm, 454.36 mW cm^{-2}) for 240 s, the transfer curves of BCP-1/$MAPbBr_3$ and BCP-2/$MAPbBr_3$ based photomemories remarkably shifted to the positive region, indicating the electron-trapping capability of perovskite induced by illumination. The positive shift of transfer curves resulted in large current switching ratios of 1.51×10^4 and 2.94×10^2 for BCP-1/$MAPbBr_3$ and BCP-2/$MAPbBr_3$, respectively, at $V_{GS} = 0$ V. The photo-writing effects induced by the trapped carriers in the hybrid film can be further erased by applying a gate bias at −60 V for 1 s and the threshold voltage (V_{th}) can be shifted back to its initial state as a result of charge neutralization enabled by the injected holes.

In contrast, as shown in Figure S6a,b, Supporting Information, the reference devices with PS/$MAPbBr_3$ and PEO/$MAPbBr_3$ as the photo-induced charge storage layer showed deteriorated field-effect modulated current with extremely high OFF current around 10^{-8} A. Thus, the indistinguishable ON/OFF current ratio for both reference devices after light illumination can be observed (Figure S6c,d, Supporting Information). Those observations may result from the fact that homopolymer cannot accommodate large amount of perovskite, and thus excess perovskite phase accumulated on the surface of composite film and formed a continuous network, as shown in the SEM images (Figure S2c,d, Supporting Information) which resulted in the rough surface composite films and correspondingly deteriorated electrical performance of the semiconductor layer. The significant difference in homopolymer and BCP system highlight the pivotal role of BCP as the template for spatially-addressable perovskite-based photomemory.

To further elucidate the photon-writing phenomena, the temporal response of the drain current (I_{DS}) under green-light illumination (520 nm, 454.36 mW cm^{-2}) was traced by recording the I_{DS} at a fixed $V_{DS} = -60$ V and $V_{GS} = 0$ V. Figure S7a, Supporting Information, shows that the I_{DS} initially maintained a low conductive state ($\approx 10^{-12}$ A) in the dark, and abruptly increased to 10^{-7} and 10^{-8} A for BCP-1/$MAPbBr_3$ and BCP-2/$MAPbBr_3$, respectively. Even after removing the illumination (at 240 s), the I_{DS} can still maintain the same order. Figure S7b, Supporting Information, shows the same measurement at low consumption voltage at $V_{DS} = -5$ V and $V_{GS} = 0$ V. Benefiting from the high mobility of P3HT, the derived BCP-1/$MAPbBr_3$ and BCP-2/$MAPbBr_3$ device still remained non-volatile under a small V_{DS} of −5 V. Notably, the BCP-1/$MAPbBr_3$ system exhibited a higher photocurrent than the BCP-2/$MAPbBr_3$ system. This is reasonably speculated to be related to the higher

© 2020 WILEY-VCH Verlag GmbH & Co. KGaA, Weinheim

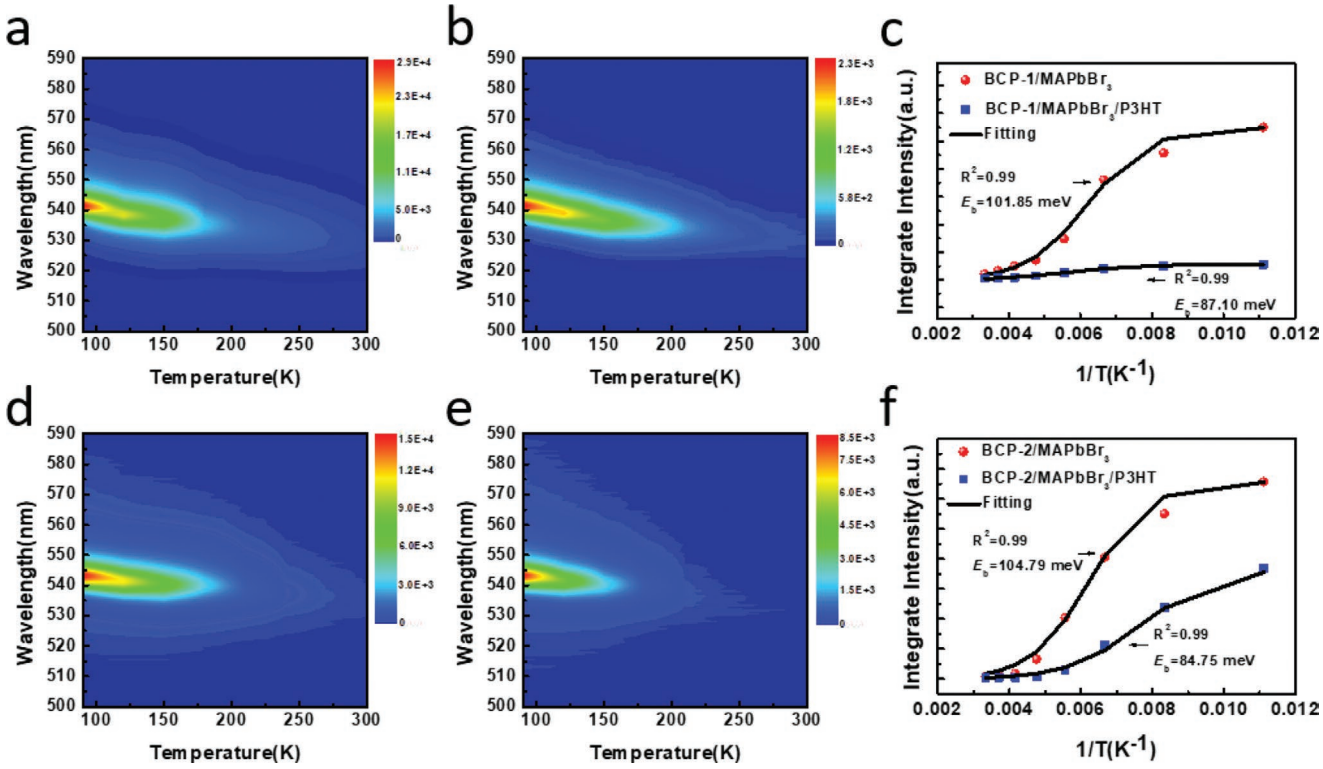

Figure 4. Pseudocolor maps of temperature-dependent PL spectra of a) BCP-1/$MAPbBr_3$ and b) BCP-1/$MAPbBr_3$/P3HT. c) Temperature-dependent PL spectra BCP-1/$MAPbBr_3$ and BCP-1/$MAPbBr_3$/P3HT. Pseudocolor maps of temperature-dependent PL spectra of d) BCP-2/$MAPbBr_3$ and e) BCP-2/$MAPbBr_3$/P3HT. f) Temperature-dependent PL spectra of BCP-2/$MAPbBr_3$ and BCP-2/$MAPbBr_3$/P3HT.

interfacial contact area between the perovskite domain and the P3HT film.

Long-term storage capability is an important index for non-volatile photomemory. Figure S7c, Supporting Information, shows the long-term measurement of BCP-1/$MAPbBr_3$ and BCP-2/$MAPbBr_3$ as light-trapping dielectric layers. After 240 s of illumination, the current remained stable for 40 000 s, affirming the isolating effect of BCP in the composite film under high composition of perovskite in composite film.

Temporal photocurrents of the studied photomemory under different light sources and illumination intensities were implemented. Figure S8a,b, Supporting Information, shows the dependence of the photocurrents obtained by the BCP-1/$MAPbBr_3$ and BCP-2/$MAPbBr_3$ derived photomemories under different intensities of 450 nm wavelength illumination for 240 s, respectively. The temporal I_{DS} curves at V_{DS} = −60 V with varying illumination intensities from 0.48 to 1822.31 mW cm^{-2} still resulted in an extremely high current. As the intensity decreased, the current maintenance was observed after illumination in the BCP-1/$MAPbBr_3$ system, but a slight decrease was observed in the BCP-2/$MAPbBr_3$ system. These phenomena were more pronounced under green-light (Figure S8c,d, Supporting Information) and red-light illumination (Figure S8e,f, Supporting Information). The higher photocurrent in the BCP-1/$MAPbBr_3$ system regardless of wavelength and illumination intensity inferred that the larger interfacial area between $MAPbBr_3$ and P3HT improved the light sensitivity and photo-induced charge storage capability as well. Besides, it is interesting to note that due to the anti-solvent characteristic of composite film and the complementary absorption of $MAPbBr_3$ and conjugated polymer, the broadband photosensitive photomemory covered from blue-light to red-light region can be realized to allow big data transmission on Li-Fi application.

To further explore the morphological effect on the kinetic mechanism of the charge transfer between $MAPbBr_3$ and P3HT, various photo-writing time ranged from 5 ms to 240 s were executed with wavelength of 520 nm and light intensity of 454.36 mW cm^{-2}. As shown in Figure 5c, the photocurrent of BCP-1/$MAPbBr_3$ system showed consistent photocurrent response in the photo-programming time ranging from 1 to 240 s, demonstrating the rapid charge transfer rate. As the photo-programming time decreased from 1 s to 5 ms, the photocurrent is suddenly dropped to 10^{-10} A but still demonstrated a superior memory functionality even under 5 ms illumination. In striking contrast to this, in the BCP-2/$MAPbBr_3$ system (Figure 5d), the photocurrent was slightly deteriorated when the photo-programming time decreased from 240 to 1 s. As the illumination time shifted to the range of 0.1 s to 5 ms, only temporary current response was observed. Figure 5e summarizes the relationship between the above photo-induced current response toward photo-programming time, which demonstrated that the BCP-1/$MAPbBr_3$ system maintained a decent charge storage capability with an ON/OFF ratio of one order under an extremely short photo-programming time of 5 ms, whereas the illumination time of 1 s is the minimum photo-programming time for the non-volatile memory effect in the BCP-2/$MAPbBr_3$ system.

© 2020 WILEY-VCH Verlag GmbH & Co. KGaA, Weinheim

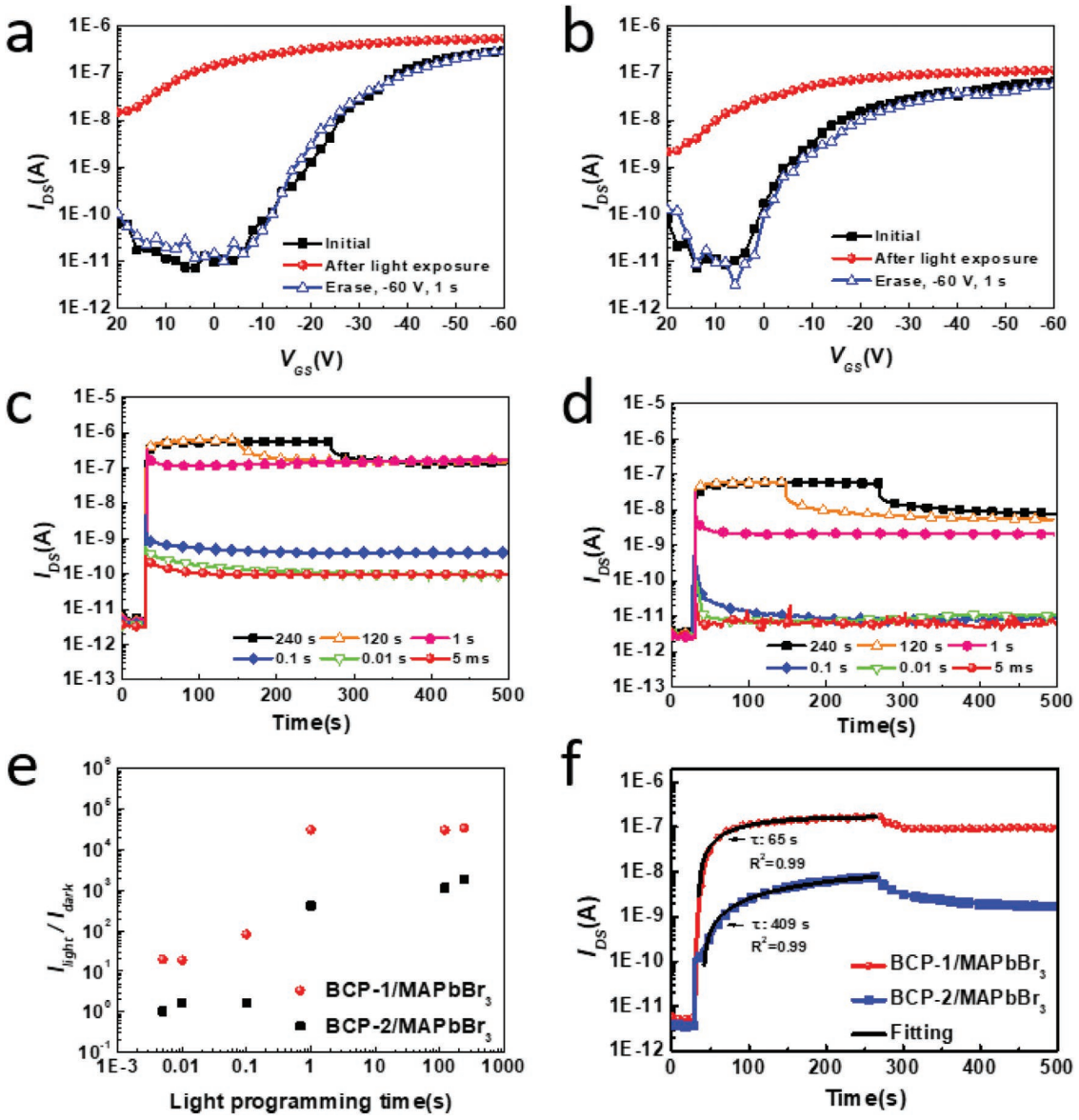

Figure 5. Photo-programming characteristics of the studied photomemory. Transfer characteristic of the perovskite-based photomemory at V_{DS} = –60 V: a) BCP-1/MAPbBr$_3$, b) BCP-2/MAPbBr$_3$. Temporal I_{DS} curves at V_{DS} = –60 V with different illuminating time ranging from 5 ms to 240 s: c) BCP-1/MAPbBr$_3$, d) BCP-2/MAPbBr$_3$. e) Photocurrent current/dark current ratio toward illumination time diagram. f) The photo-responsive current toward time under weaker green-light illumination (520 nm, 0.4 mW cm^{-2}) at V_{DS} = –60 V for BCP-1/MAPbBr$_3$ and BCP-2/MAPbBr$_3$ derived photomemory.

The switching stability of the BCP-1/MAPbBr$_3$-based photomemory was evaluated using sequential optical writing–reading–electrical erasing–reading (WRER) cycles (Figure S7d, Supporting Information). The operating conditions of WRER cycles were fixed at V_{DS} = –60 V, while the optical writing and reading processes were implemented at V_{GS} = 0 V. During photogating (520 nm, 454.36 mW cm^{-2}) for 1 s, the I_{DS} can rapidly increase from 10^{-12} to 10^{-7} A and then remain constant after removing the excitation light. Once erased by applying a V_{GS} of –60 V, the I_{DS} would return to the original low current state.

To further clarify the dynamics of photo-induced charge transfer process for both BCP/MAPbBr$_3$ systems, the photo-responsive current toward time under weak green-light illumination (520 nm, 0.4 mW cm^{-2}) at V_{DS} = –60 V was executed (Figure 5f) and described by Equation (2).

$$I = A\left(1 - \exp\left(\frac{-t}{\tau}\right)\right) + I_{\text{dark}} \tag{2}$$

where t is time, τ is the time constant, I_{dark} is the dark current, and A is the scaling constant. The time constants for the rising part of the photocurrent are 65 and 409 s for BCP-1/MAPbBr$_3$ and BCP-2/MAPbBr$_3$ derived photomemories, respectively. To confirm the dynamics of photo-induced charge transfer process for both BCP/MAPbBr$_3$ systems in broad spectrum, Figures S9a and S9b, Supporting Information, show the

© 2020 WILEY-VCH Verlag GmbH & Co. KGaA, Weinheim

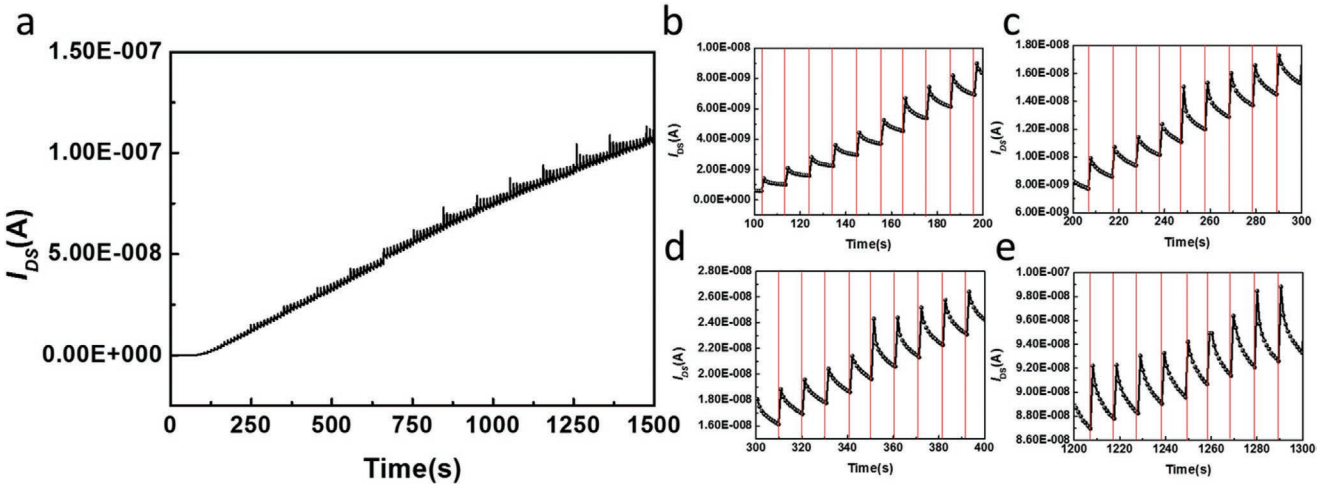

Figure 6. The multilevel behavior of the BCP-1/$MAPbBr_3$-derived photomemory at V_{DS} = −60 V with illuminating time of 5 ms laser pulses (520 nm, 454.36 mW cm^{-2}) for every 10 s. Multilevel memory behavior capability at time interval of a) 0–1500 s, b) 100–200 s, c) 200–300 s, d) 300–400 s, and e) 1200–1300 s.

photo-responsive current toward time under weak blue-light illumination (450 nm, 0.5 mW cm^{-2}) and weak red-light illumination (650 nm, 0.8 mW cm^{-2}) at V_{DS} = −60 V, respectively. Consistently, the time constant of BCP-1/$MAPbBr_3$ is shorter than the one of BCP-2/$MAPbBr_3$. When considering that weight composition of perovskite in composite film are the same for both BCP/$MAPbBr_3$ systems, the shorter τ is indicative of faster charge transfer rate probably due to the larger interfacial area between $MAPbBr_3$ and P3HT in the BCP-1/$MAPbBr_3$ system.[37,38] So far, limited studies have addressed the photo-programming time which is an essential parameter to meet the requirement of mass computation and big data.

A typical memory device features limited two-level memory characteristics, resulting in a cell that can only store one bit of information. Benefitting from the ultrafast photo-programmable BCP-1/$MAPbBr_3$-derived photomemory, multilevel behavior can be achieved. As shown in **Figure 6**a, the BCP-1/$MAPbBr_3$ derived photomemory was operated at V_{DS} = −60 V with an illuminating time of 5 ms laser pulses (at 520 nm, 454.36 mW cm^{-2}) every 10 s. The I_{DS} can be superimposed by continuous pulses due to the non-volatile functionality of prepared photomemory, and according to the different time interval of the photocurrent in Figure 6b–e, a data storage capacity of over 7 bits (128 levels) in one cell can be achieved.

2.4. Dynamics Analysis of Charge-Carrier Transfer Efficiency

If the assumption is made that charge transfer rate dominated the time constant of the photocurrent, then the critical issue is to identify the nature of exciton lifetime of perovskite in the block copolymer matrix. To elucidate the morphological difference of BCP/$MAPbBr_3$ composite film on the resulting exciton recombination dynamics, time-resolved PL spectra were measured. The 2D contour plots of the time-resolved photoluminescence (TRPL) spectra of the BCP-1/$MAPbBr_3$ and BCP-2/$MAPbBr_3$ films are presented in **Figures 7**a and 7d, respectively, while the one for the BCP-1/$MAPbBr_3$/P3HT film and BCP-2/$MAPbBr_3$/P3HT film are presented in Figures 7b and 7e, respectively, for comparison. The corresponding fluorescence decay curves at a wavelength of 530 nm are displayed in Figure 7c,f for BCP-1/$MAPbBr_3$ and BCP-1/$MAPbBr_3$ systems without and with P3HT films. The PL decay can be described by biexponential fitting (Equation (3)), providing the short-lived PL lifetime (τ_1) and long-lived PL lifetime (τ_2).

$$A(t) = A_1 \exp\left(\frac{-t}{\tau_1}\right) + A_2 \exp\left(\frac{-t}{\tau_2}\right) \tag{3}$$

The intensity-averaged decay time can be described using Equation (4), and it can be resolved into the dynamics of a charge transfer rate (k_{CT}) and charge transfer efficiency (CTE) between BCP/$MAPbbr_3$ composite films to the P3HT layers expressed using Equations (5) and (6).[39–41]

$$\tau_{\text{average}} = \frac{\sum_{i=1}^{n} A_i \tau_i}{\sum_{i=1}^{n} A_i} \tag{4}$$

$$\frac{1}{\tau_{\text{P3HT/composite film}}} = \frac{1}{\tau_{\text{composite film}}} + \frac{1}{\tau_{\text{CT}}}; k_{\text{CT}} = \tau_{\text{CT}}^{-1} \tag{5}$$

$$\text{CTE} = \frac{\tau_{\text{composite film}} - \tau_{\text{P3HT/composite film}}}{\tau_{\text{composite film}}} \times 100\% \tag{6}$$

All parameters are summarized in Table S1, Supporting Information. The average fluorescence decay time of the BCP-1/$MAPbBr_3$ film remarkably decreased from 135 to 15 ns as the composite film contacted with P3HT film with CTE of 89% and k_{CT} of 0.056 ns^{-1}. By contrast, the inferior CTE (43%) and k_{CT} (0.018 ns^{-1}) in the case of BCP-2/$MAPbBr_3$ system indicate that the insulating PS between perovskite and P3HT not only thermodynamically reduced the photocurrent of the derived photomemory but also dynamically inhibited the photo-induced charge transfer. Compared to perovskite spheres in the BCP-2/$MAPbBr_3$ film, the perovskite domain

© 2020 WILEY-VCH Verlag GmbH & Co. KGaA, Weinheim

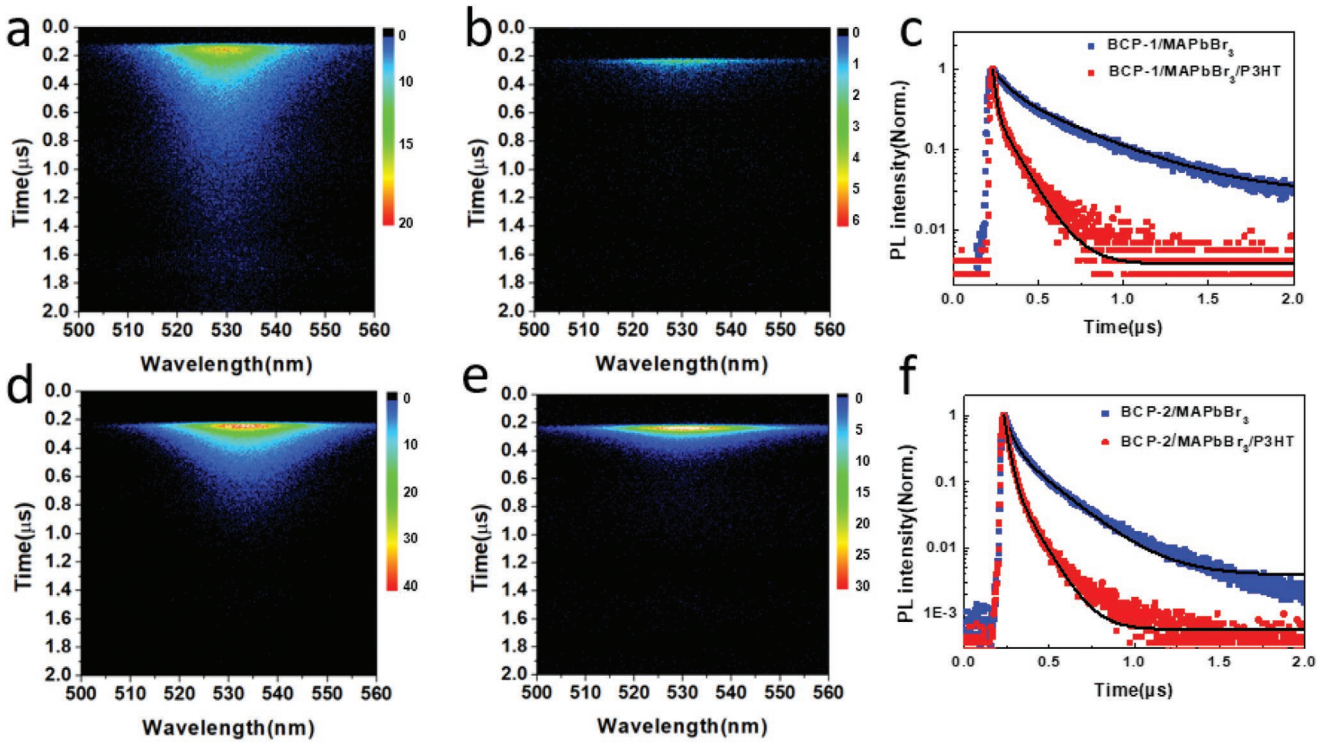

Figure 7. 2D spectra of TRPL of a) BCP-1/$MAPbBr_3$ and b) BCP-1/ $MAPbBr_3$/P3HT. c) TRPL decay with the fitting curves of BCP-1/$MAPbBr_3$ and BCP-1/$MAPbBr_3$/P3HT. 2D spectra of TRPL of d) BCP-2/$MAPbBr_3$ and e) BCP-2/$MAPbBr_3$/P3HT. f) TRPL decay with the fitting curves of BCP-2/$MAPbBr_3$ and BCP-2/$MAPbBr_3$/P3HT.

in the BCP-1/$MAPbBr_3$ film directly exposed to the P3HT film favored hole transfer and consequently possessed higher charge transfer rate. Besides, it is interesting to note that the exciton lifetime of perovskite in BCP/$MAPbBr_3$ film is related to the molar ratios between PEO segment and perovskite with values of 135 and 42 ns for BCP-1/$MAPbBr_3$ and BCP-2/$MAPbBr_3$, respectively. According to the study of surface-related emission in highly luminescent perovskites, the longer exciton lifetime of perovskite in BCP-1/$MAPbBr_3$ could be attributed to the fact that the PEO provide the healing effect for the defect site on the surface of the perovskite grain which inhibit the non-radiative pathway.[34–36]

2.5. Mechanism of the Studied Photomemory

Based on the above electrical properties and the corresponding photo-physical analyses, the plausible operating mechanism of BCP/$MAPbBr_3$-based photomemory was proposed as illustrated in **Figure 8**a. Under blue- or green-light illumination, photo-excited electrons and holes are generated within perovskite. Because of the energy level difference between perovskite and P3HT, the holes would transfer to the P3HT and serve as charge-carriers in the active channel while the electrons would be trapped in the noncontinuous perovskite phase to inhibit the trapped charge dissipation. The photo-programmed photomemory can be further erased by applying negative gate bias to prompt the hole injection from P3HT to perovskite. On the other hand, under red-light illumination, the photo-excited electrons in P3HT would transfer to the perovskite as trapping charges in the noncontinuous perovskite phase. The electric field driven erasing process could be realized by applying negative gate bias to prompt the hole injection from P3HT

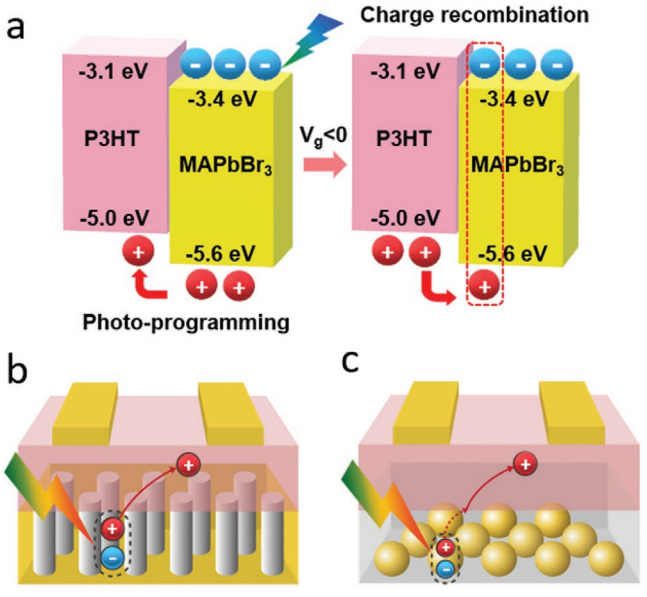

Figure 8. a) Schematic diagram of operating mechanism under blue- and green-light illumination. Schematic diagrams of charge transfer process between BCP/$MAPbBr_3$ composite films and P3HT for b) BCP-1/$MAPbBr_3$ and c) BCP-2/$MAPbBr_3$ derived photomemory.

© 2020 WILEY-VCH Verlag GmbH & Co. KGaA, Weinheim

to perovskite (Figure S10, Supporting information). Both the BCP-1/$MAPbBr_3$ and BCP-2/$MAPbBr_3$ based photomemories followed the above mechanism; however, due to the morphological difference in the two varying block ratios of PS-*b*-PEO, the large interfacial area and direct contact between the perovskite/PEO and the P3HT in BCP-1/$MAPbBr_3$ endow the derived photomemory with higher photocurrent and faster charge transfer rate between the perovskite and the P3HT. By contrast, the PS segment in the BCP-2/$MAPbBr_3$ composite film served as an insulating matrix between the perovskite/PEO and the P3HT which inhibited the charge transfer and consequently deteriorated the photocurrent and charge transfer rate.

3. Conclusion

In summary, the spatially addressable perovskite in PS-*b*-PEO/perovskite composite film as photoactive floating gate was demonstrated to elucidate the effect of morphology on the photo-responsive characteristics of photomemory for the first time. The anti-solvent properties of PS-*b*-PEO/perovskite composite film enabled the solution-processable conjugated polymer as active channel to broaden the absorption spectrum. Through manipulating the interfacial area between perovskite and active channel in terms of the volume fraction of PS and PEO segments, fast photo-induced charge transfer rate of 0.056 ns^{-1}, high CTE of 89%, ON/OFF current ratio of 10^4, and extremely low programming time of 5 ms can be achieved.

4. Experimental Section

Materials: Lead(II) bromide ($PbBr_2$) (99.999% trace metals basis), methylammonium bromide (MABr) (98%, powder), polystyrene (analytical standard for GPC, average M_w 400 000 g mol^{-1}), PEO (average M_w 400 000 g mol^{-1}), *N*,*N*-dimethylformamide (anhydrous, 99.8%), and toluene (anhydrous, 99.8%) were purchased from Sigma-Aldrich. Two linear PS-*b*-PEO block copolymers (M_n(PS) = 24 000 g mol^{-1}, M_n(PEO) = 21 000 g mol^{-1}; M_w/M_n = 1.09 and M_n(PS) = 114 000 g mol^{-1}, M_n(PEO) = 31 000 g mol^{-1}; M_w/M_n = 1.18, respectively), were purchased from Polymer Source, Inc., Canada. Poly(3-hexylthiophene) (P3HT) ($M_w \approx$ 50 000, 90–95% regioregular) was obtained from Rieke Metals Inc.

Fabrication of Photomemory: The precursor solution of perovskite was made by dissolving 1 mmol $PbBr_2$ and 1 mmol CH_3NH_3Br in 1 mL DMF. First, the highly doped n-type Si (100) wafer with a 100-nm-thick SiO_2 was cleaned in toluene, acetone, and isopropanol by sonication for 20 min. Polymer/perovskite hybrid solutions (with concentration of 10 mg mL^{-1}:24 mg mL^{-1}) were spin-cast (1000 rpm, 60 s) on a wafer and then solvent annealed under saturated benzene vapor for 17 h in N_2-filled glove box at room temperature. The P3HT solution was prepared in toluene with a concentration of 1 mg mL^{-1} and spin-cast onto the polymer/perovskite layer. Top-contact gold electrodes (50 nm) were subsequently deposited by evaporation through a shadow mask with a channel length (L) and width (W) of 50 and 1000 µm, respectively.

Characterization: To identify the interaction between polymer and perovskite, FTIR (Miracle ATR, Perkin Elmer) and TEM (JEM-2100F Electron Microscope) were operated to investigate the morphology of nanostructured perovskite in the polymer matrix. The surface images of composite films were observed using a SEM (Hitachi, S-4800-I). All samples were sputtered with platinum. The UV–vis absorption spectra were obtained using a Shimadzu UV-2600 spectrometer. GISAXS at Taiwan Light Source (TLS) beamline 23A and GIWAXS at TLS beamline 13A were performed to investigate the ordered structure of composite films and perovskite crystals in the National Synchrotron Radiation Research Center (NSRRC), Taiwan. Temperature-dependent photoluminescence measurements were executed at 325 nm wavelength under He-Cd laser excitation with an average power of 45 mW in the cryogenic system. The TRPL spectra were excited at wavelength of 375 nm and collected using a fiber, coupled with Hamamatsu C10910 streak camera and M10913 slow single-sweep unit at the NSRRC, Taiwan.

In order to measure the electrical properties of photomemory, all measurements were conducted using a Keithley 4200-SCS semiconductor parameter analyzer in a nitrogen-filled glove box at room temperature. The photomemory with a wide absorption wavelength allowed to measure photocurrents with various light sources (450 nm laser with intensity of 0.48 to 1822.31 mW cm^{-2}, 520-nm laser with intensity of 0.40 to 454.36 mW cm^{-2}, and 650 nm laser with intensity of 0.79 to 1306.19 mW cm^{-2}). The intensity and pulse width of laser sources were adjusted using Keithley 2602.

Supporting Information

Supporting Information is available from the Wiley Online Library or from the author.

Acknowledgements

The authors thank the financial support from the Ministry of Science and Technology (MOST) in Taiwan (MOST 108-2636-E-194-001 and MOST 109-2636-E-194-001) and the Advanced Institute of Manufacturing with High-tech Innovations from The Featured Areas Research Center Program within the framework of the Higher Education Sprout Project by the Ministry of Education (MOE) in Taiwan. The authors also gratefully appreciate the Center for Micro/Nano Science and Technology, National Cheng Kung University, for the transmission electron microscopy analysis and Dr. Bi-Hsuan Lin at National Synchrotron Radiation Research Center for the help of time-solved photoluminescence analysis.

Conflict of Interest

The authors declare no conflict of interest.

Keywords

block copolymers, floating-gate photomemory, multi-level memory, organic–inorganic hybrid perovskite

Received: January 26, 2020
Revised: March 4, 2020
Published online: April 6, 2020

[1] H. Haas, *Rev. Phys.* **2018**, *3*, 26.
[2] H. Haas, L. Yin, Y. Wang, C. Chen, *J. Lightwave Technol.* **2016**, *34*, 1533.
[3] D. Kahng, S. M. Sze, *Bell Syst. Tech. J.* **1967**, *46*, 1288.
[4] C.-C. Shih, Y.-C. Chiu, W.-Y. Lee, J.-Y. Chen, W.-C. Chen, *Adv. Funct. Mater.* **2015**, *25*, 1511.
[5] K.-J. Baeg, Y.-Y. Noh, H. Sirringhaus, D.-Y. Kim, *Adv. Funct. Mater.* **2010**, *20*, 224.
[6] J.-Y. Chen, H.-C. Hsieh, Y.-C. Chiu, W.-Y. Lee, C.-C. Hung, C.-C. Chueh, W.-C. Chen, *J. Mater. Chem. C* **2020**, *8*, 873.
[7] H. L. Park, H. Kim, D. Lim, H. Zhou, Y. H. Kim, Y. Lee, S. Park, T. W. Lee, *Adv. Mater.* **2020**, *32*, 1906899.

 © 2020 WILEY-VCH Verlag GmbH & Co. KGaA, Weinheim

[8] Y. Zhai, X. Yang, F. Wang, Z. Li, G. Ding, Z. Qiu, Y. Wang, Y. Zhou, S.-T. Han, *Adv. Mater.* **2018**, *30*, 1803563.
[9] M. K. Dai, Y. R. Liou, J. T. Lian, T. Y. Lin, Y. F. Chen, *ACS Photonics* **2015**, *2*, 1057.
[10] Y. J. Jeong, D. J. Yun, S. H. Kim, J. Jang, C. E. Park, *ACS Appl. Mater. Interfaces* **2017**, *9*, 11759.
[11] T. Leydecker, M. Herder, E. Pavlica, G. Bratina, S. Hecht, E. Orgiu, P. Samorì, *Nat. Nanotechnol.* **2016**, *11*, 769.
[12] N. Ahn, D.-Y. Son, I.-H. Jang, S. M. Kang, M. Choi, N.-G. Park, *J. Am. Chem. Soc.* **2015**, *137*, 8696.
[13] P.-W. Liang, C.-Y. Liao, C.-C. Chueh, F. Zuo, S. T. Williams, X.-K. Xin, J. Lin, A. K.-Y. Jen, *Adv. Mater.* **2014**, *26*, 3748.
[14] L. Meng, J. You, T.-F. Guo, Y. Yang, *Acc. Chem. Res.* **2016**, *49*, 155.
[15] N.-G. Park, *Mater. Today* **2015**, *18*, 65.
[16] B. Saparov, D. B. Mitzi, *Chem. Rev.* **2016**, *116*, 4558.
[17] S. D. Stranks, G. E. Eperon, G. Grancini, C. Menelaou, M. J. P. Alcocer, T. Leijtens, L. M. Herz, A. Petrozza, H. J. Snaith, *Science* **2013**, *342*, 341.
[18] R. Younts, H.-S. Duan, B. Gautam, B. Saparov, J. Liu, C. Mongin, F. N. Castellano, D. B. Mitzi, K. Gundogdu, *Adv. Mater.* **2017**, *29*, 1604278.
[19] J. Huang, Y. Yuan, Y. Shao, Y. Yan, *Nat. Rev. Mater.* **2017**, *2*.
[20] J.-Y. Chen, Y.-C. Chiu, Y.-T. Li, C.-C. Chueh, W.-C. Chen, *Adv. Mater.* **2017**, *29*, 1702217.
[21] E. Ercan, J.-Y. Chen, C.-C. Shih, C.-C. Chueh, W.-C. Chen, *Nanoscale* **2018**, *10*, 18869.
[22] H.-Y. Chi, H.-W. Hsu, S.-H. Tung, C.-L. Liu, *ACS Appl. Mater. Interfaces* **2015**, *7*, 5663.
[23] H. K. Lin, Y. W. Su, H. C. Chen, Y. J. Huang, K. H. Wei, *ACS Appl. Mater. Interfaces* **2016**, *8*, 24603.
[24] M. Kang, K. J. Baeg, D. Khim, Y. Y. Noh, D. Y. Kim, *Adv. Funct. Mater.* **2013**, *23*, 3503.
[25] W. L. Leong, P. S. Lee, A. Lohani, Y. M. Lam, T. Chen, S. Zhang, A. Dodabalapur, S. G. Mhaisalkar, *Adv. Mater.* **2008**, *20*, 2325.
[26] J. C. Chen, C. L. Liu, Y. S. Sun, S. H. Tung, W. C. Chen, *Soft Matter* **2012**, *8*, 526.
[27] C. M. Chen, C. M. Liu, K. H. Wei, U. S. Jeng, C. H. Su, *J. Mater. Chem.* **2012**, *22*, 454.
[28] Y. J. Yoon, Y. H. Chen, J. Jung, Y. J. Chang, C. H. Lin, S. T. Yu, S. G. Zhang, C. H. Lu, S. Pan, Z. W. Wang, Z. T. Kang, V. Tsukruk, Z. Q. Lin, *Abstr. Pap. Am. Chem. Soc.* **2018**, *256*.
[29] S. C. Hou, Y. Z. Guo, Y. G. Tang, Q. M. Quan, *ACS Appl. Mater. Interfaces* **2017**, *9*, 18417.
[30] L. A. Dubraja, R. Kruk, T. Brezesinski, *Adv. Electron. Mater.* **2019**, *5*.
[31] H. Han, B. Jeong, T. H. Park, W. Cha, S. M. Cho, Y. Kim, H. H. Kim, D. Kim, D. Y. Ryu, W. K. Choi, C. Park, *Adv. Funct. Mater.* **2019**, *29*, 1808193.
[32] S. M. Lee, H. Jung, W. I. Park, Y. Lee, E. Koo, J. Bang, *ChemistrySelect* **2018**, *3*, 11320.
[33] N. J. Zhou, Y. Bekenstein, C. N. Eisler, D. D. Zhang, A. M. Schwartzberg, P. D. Yang, A. P. Alivisatos, J. A. Lewis, *Sci. Adv.* **2019**, *5*.
[34] H. P. Dong, Y. Li, S. F. Wang, W. Z. Li, N. Li, X. D. Guo, L. D. Wang, *J. Mater. Chem. A* **2015**, *3*, 9999.
[35] M. Kim, S. G. Motti, R. Sorrentino, A. Petrozza, *Energy Environ. Sci.* **2018**, *11*, 2609.
[36] Y. Zhao, J. Wei, H. Li, Y. Yan, W. Zhou, D. Yu, Q. Zhao, *Nat. Commun.* **2016**, *7*, 10228.
[37] C. Fan, Q. Yue, J. Yang, Z. Wei, S. Yang, J. Li, *Appl. Phys. Lett.* **2014**, *104*, 202105.
[38] C. Liu, A. Piyadasa, M. Piech, S. Dardona, Z. Ren, P.-X. Gao, *J. Mater. Chem. C* **2016**, *4*, 6176.
[39] K.-S. Cho, K. Heo, C.-W. Baik, J. Y. Choi, H. Jeong, S. Hwang, S. Y. Lee, *Nat. Commun.* **2017**, *8*, 840.
[40] K.-H. Lin, C.-Y. Chuang, Y.-Y. Lee, F.-C. Li, Y.-M. Chang, I. P. Liu, S.-C. Chou, Y.-L. Lee, *J. Phys. Chem. C* **2012**, *116*, 1550.
[41] S. Bae, J.-S. Park, I. K. Han, T. J. Shin, W. H. Jo, *Sol. Energy Mater. Sol. Cells* **2017**, *160*, 77.

© 2020 WILEY-VCH Verlag GmbH & Co. KGaA, Weinheim